

Finite Element Analysis of a Novel Design of a Three Phase Transverse Flux Machine With an External Rotor

Erich Schmidt

Institute of Energy Systems and Electric Drives, Vienna University of Technology, Vienna 1040, Austria

The permanent magnet excited transverse flux machine is well suited in particular for direct drive applications of electric road vehicles. The novel single-sided design with an external rotor consists of a three phase arrangement with a total number of 120 poles. The 3D finite element model with completely independent rotor and stator parts includes only two poles of the machine with appropriate repeating periodic boundary conditions for the unknown degrees of freedom of the 3D magnetic vector potential. Thus, the various angular rotor positions can be calculated by utilizing the sliding surface approach and a domain decomposition algorithm. The results presented herein are focussed on the most important design parameters such as electromagnetic torque, no-load voltages and short-circuit currents.

Index Terms—Finite element analysis, permanent magnet machine, transverse flux machine.

I. INTRODUCTION

THE transverse flux machine with a permanent magnet excited external rotor is one of the most important machine topology for the application with wheel hub drive systems of electric driven vehicles. In general, two different topologies of a transverse flux machine exist [1]–[5]. Thereby, double-sided arrangements can be used only in either single phase or two phase mode. On the other hand, single-sided arrangements can be designed for three phase mode, too.

In contrast to conventional induction machines with more than one phase, there is no common rotating field with all designs of transverse flux machines [1]–[6]. In order to produce a resulting shaft torque as comparatively as smooth as with conventional induction machines, either stator or rotor parts have to be mechanically shifted according to the number of phases. Nevertheless, the alternating fields with an electrical angular shift according to the number of phases cause higher harmonics with the electromagnetic torque as well as noticeable shear stresses in all carrier parts and the shaft.

The single-phase basic arrangement of two poles of the novel single-sided topology is depicted in Fig. 1. On the other hand, Fig. 2 shows two poles of the three phase arrangement with an external rotor. The rotor parts of the three phases are arranged in line and carry the permanent magnets with an alternating magnetization in circumferential direction. The stator parts of the three phases carry the ring windings of the three phases and have an appropriate mechanical angular shift necessary for the three phase operation.

In order to setup an environment suitable for the prototype design with its main data listed in Table I, special attention will be given to both 3D finite element modelling and analysis methods. With the intended application of the prototype design with electric road vehicles, the evolved electromagnetic torque of the machine will be most essential. Additionally, no-load voltages and short-circuit currents are the most important design criteria for the complete drive system.

Manuscript received May 31, 2010; revised August 09, 2010; accepted September 22, 2010. Date of current version April 22, 2011. Corresponding author: E. Schmidt (e-mail: erich.schmidt@tuwien.ac.at).

Color versions of one or more of the figures in this paper are available online at <http://ieeexplore.ieee.org>.

Digital Object Identifier 10.1109/TMAG.2010.2084075

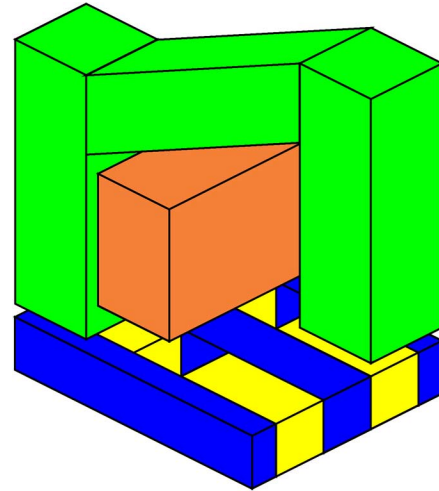


Fig. 1. Basic arrangement of two poles of a single sided transverse flux machine with flux concentration.

II. FINITE ELEMENT MODELLING

The various nonlinear finite element analyses utilize a formulation with a 3D vector potential \mathbf{A} and an incorporated Coulomb gauge

$$\text{curl}(\varrho \cdot \text{curl} \mathbf{A}) = \mathbf{J}, \quad \text{div} \mathbf{A} = 0 \quad (1)$$

with appropriate Neumann and Dirichlet boundary conditions

$$(\varrho \cdot \text{curl} \mathbf{A}) \times \mathbf{n} = \mathbf{K} \quad \text{on } \Gamma_H \quad (2a)$$

$$\mathbf{A} \times \mathbf{n} = \mathbf{0} \quad \text{on } \Gamma_B \quad (2b)$$

where ϱ denotes an anisotropic reluctivity tensor, \mathbf{J} describes the source current densities, Γ_H and Γ_B are the boundaries where the tangential magnetic field $\mathbf{n} \times \mathbf{H}$ is specified by a surface current density \mathbf{K} and where the normal magnetic flux density $\mathbf{n} \cdot \mathbf{B}$ is specified [7]–[9].

The finite element model as shown in Fig. 2 consists of completely independent stator as well as rotor parts and includes only two poles of the machine as the smallest necessary part. In order to reflect the periodicity of the magnetic field, appropriate repeating periodic boundary conditions for the unknown degrees of freedom of the 3D magnetic vector potential are applied at the boundaries being two poles pitches apart. With

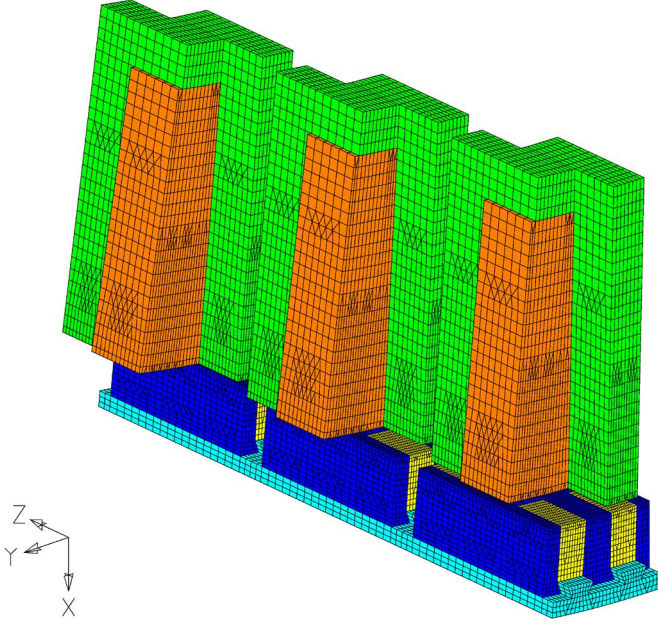


Fig. 2. Three phase transverse flux machine with inline rotor segments and inserted permanent magnets as well as shifted stator segments and ring windings, finite element model of two poles.

TABLE I
MAIN DATA OF THE TRANSVERSE FLUX MACHINE

Number of poles	120
Rated speed	400 rpm
Stator diameter	380 mm
Airgap length	1 mm
Axial length	100 mm

an intent of investigating cross-coupling effects of the phases, Dirichlet boundary conditions of the magnetic vector potential on the symmetry planes between the phases in axial direction can be used optionally. With these internal boundary conditions, the magnetic flux densities are only tangential on these symmetry planes yielding decoupled phases.

Regarding the arrangement as depicted in Fig. 2, the nonlinear anisotropic material properties of the laminated stator and rotor iron regions are described by

$$\nu_{r\varphi z}(\mathbf{B}) = \begin{bmatrix} \nu_{rr}(\mathbf{B}) & 0 & 0 \\ 0 & \nu_{\varphi\varphi}(\mathbf{B}) & 0 \\ 0 & 0 & \nu_{zz}(\mathbf{B}) \end{bmatrix}$$

$$\nu_{\varphi\varphi}(\mathbf{B}) = (1 - k_F)\nu_0 + k_F\sqrt{\nu_{rr}(\mathbf{B})\nu_{zz}(\mathbf{B})} \quad (3)$$

where k_F denotes the stacking factor of the laminations.

The injection of the three phase currents i_k , $k = 1, 2, 3$, with the ring windings of the stator in dependence on the angular rotor position φ follows:

$$i_k(\varphi) = \hat{I} \cos\left(\beta + \varphi + \varphi_0 - \frac{2\pi}{3}(k-1)\right) \quad (4)$$

where φ_0 denotes the initial angular rotor position of the first phase. As shown in Fig. 2, stator and rotor of the first phase are arranged in an unaligned position which is represented by $\varphi_0 = \pi/2$. Moreover, β denotes the current angle with respect

to the rotor fixed coordinate system. Thereby, current angles of $\beta = 0$ or $\beta = \pm\pi$ produce no resultant torque. A maximum resultant torque is generated with a current angle of $\beta = \pm\pi/2$ [6].

The various angular rotor positions are now calculated by utilizing the sliding surface approach and a domain decomposition algorithm [6], [10], [11]. Thereby, the independent stator and rotor parts have an equidistant mesh discretization in circumferential direction on the cylindrical sliding surface within the air-gap while the mesh discretization in axial direction coincides between both parts. Therefore, the finite element mesh remains completely unchanged for all angular rotor positions without any remeshing. Consequently, different numerical errors with respect to the angular rotor position are avoided. Additionally, distinct decompositions of the smaller stiffness matrices of the two independent model parts significantly reduce the calculation times for various rotor positions even in the non-linear analyses.

III. ANALYSIS RESULTS

A. Electromagnetic Torque

As described in [6], the torque calculation requires only the portions along a cylindrical surface within the air-gap. Using the radial and tangential components of the magnetic flux density and summarizing the circumferential component of the Maxwell stress vector, the electromagnetic torque T_z can be evaluated from

$$T_z = p \sum_{n=1}^{N_z} \sum_{m=1}^{N_\varphi} \frac{r_T \Delta v_{mn}}{\Delta r_T} p_{\varphi, mn},$$

$$p_{\varphi, mn} = \nu_0 B_r(r_T, \varphi_m, z_n) B_\varphi(r_T, \varphi_m, z_n) \quad (5)$$

where p is the number of pole pairs, N_φ and N_z denote the numbers of air-gap elements in circumferential and axial direction, r_T and Δr_T are radius of center of gravity and radial thickness of each hexahedral air-gap element along the cylindrical surface, and Δv_{mn} denote the finite element volume, respectively.

Fig. 3 and Fig. 4 depict the cogging torque of the three phases and the entire machine with decoupled and coupled phases, respectively. Fig. 5 shows the load torque of the three phases and the entire machine with rated stator current of $\hat{I} = 120$ A in the quadrature axis according to a maximum electromagnetic torque. Fig. 6 shows the load torque of the entire machine with various quadrature axis stator currents of $\hat{I} = 30$ A ... 150 A. Corresponding, Table II lists average value and distortion factor

$$\Delta T_z = \frac{T_{z, max} - T_{z, min}}{2T_{z, av}} \quad (6)$$

as well as measurement data from an initial prototype.

The three phases contribute to the electromagnetic torque independently with only little interaction. With coupled against decoupled phases, the cogging torque of the three phases is slightly larger while with the entire machine both cogging torque and average value of the load torque are insignificantly smaller. Due to the appropriate electrical shift of the three phase currents, the resulting shaft torque is comparatively as smooth as for conventional three phase induction machines. Nevertheless, the electromagnetic torque shows higher harmonics with in particular a significant 6th harmonic component.

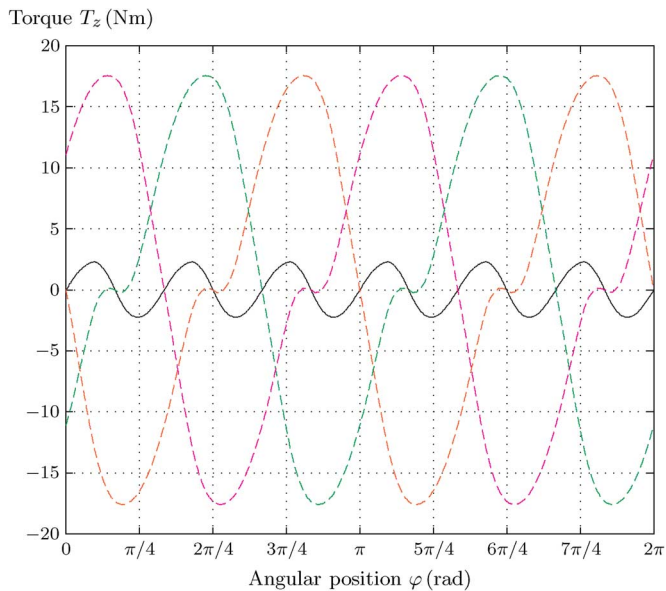


Fig. 3. Cogging torque of the three phases (dashed lines) and the entire machine (solid line), decoupled phases.

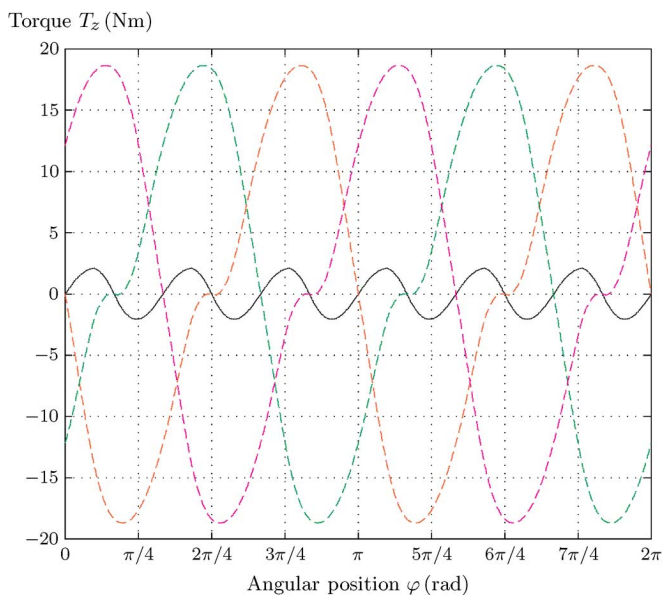


Fig. 4. Cogging torque of the three phases (dashed lines) and the entire machine (solid line), coupled phases.

B. No-Load Voltages and Short-Circuit Currents

Figs. 7 and 8 show both no-load voltages as well as short-circuit currents of the three phases for the rated speed of $n = 400$ rpm, respectively. Caused by the high level of saturation, the three phase voltages contain a significant 3rd harmonic component resulting in a non-vanishing sum of the three phase voltages as drawn additionally. On the other hand due to the low level of saturation, the three short-circuit currents of the Y-connected stator are nearly sinusoidal with respect to time. Thereby, the short-circuit currents are smaller with coupled against decoupled phases.

IV. CONCLUSION

The transverse flux machine with a permanent magnet excited rotor is well suited in particular for wheel hub drive ap-

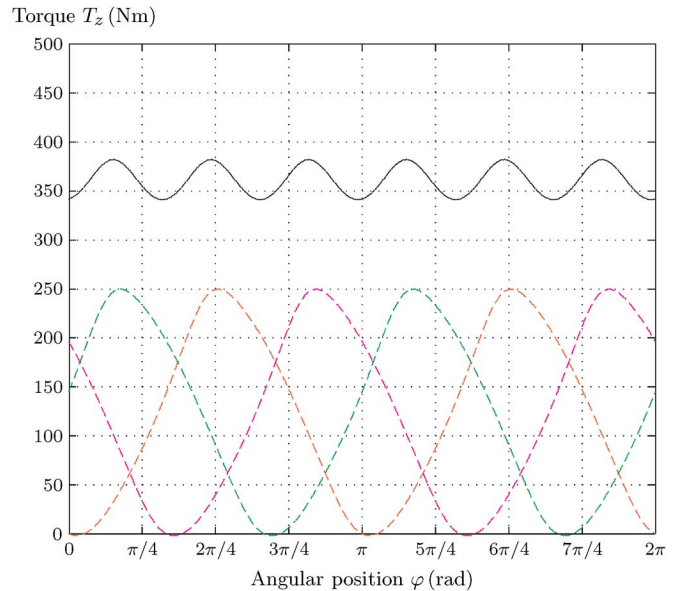


Fig. 5. Load torque of the three phases (dashed lines) and the entire machine (solid line) with rated stator current of $\hat{I} = 120$ A, coupled phases.

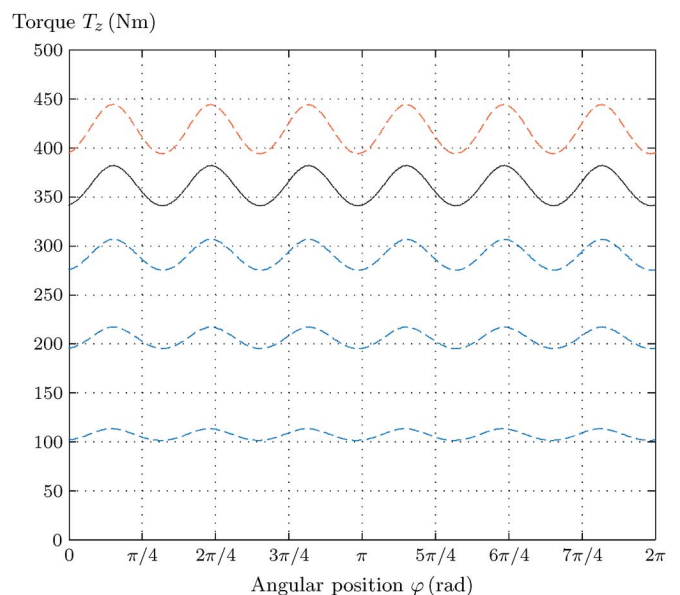


Fig. 6. Load torque of the entire machine with stator currents $\hat{I} = (30, 60, 90, 120, 150)$ A, coupled phases.

plications of electric driven vehicles. The presented novel concept of such a machine with an external rotor consists of a three phase arrangement with an appropriate mechanical angular shift of the stator parts whereas the rotor parts are arranged in line. All phases contribute to the electromagnetic torque independently with only less interaction. Due to an appropriate electrical shift of the three phase currents in the stator ring windings, the resulting shaft torque is comparatively as smooth as with conventional induction machines.

The 3D finite element analyses of the single sided transverse flux machine use only one finite element model for all angular rotor positions. This finite element model consists of completely independent rotor and stator parts. On the sliding surface between both parts, they are modelled with an equidistant finite element discretization with respect to the movement direction

TABLE II
LOAD TORQUE, AVERAGE VALUE, DISTORTION AND MEASUREMENT DATA

Current load \hat{I} (A)	Decoupled phases		Coupled phases		Measure- ment data $T_{z,m}$ (Nm)
	Average value $T_{z,av}$ (Nm)	Distortion factor ΔT_z (1)	Average value $T_{z,av}$ (Nm)	Distortion factor ΔT_z (1)	
30	109	0.0550	107	0.0555	104
60	209	0.0520	206	0.0535	196
90	295	0.0530	291	0.0540	269
120	366	0.0550	361	0.0565	325
150	425	0.0585	419	0.0600	367

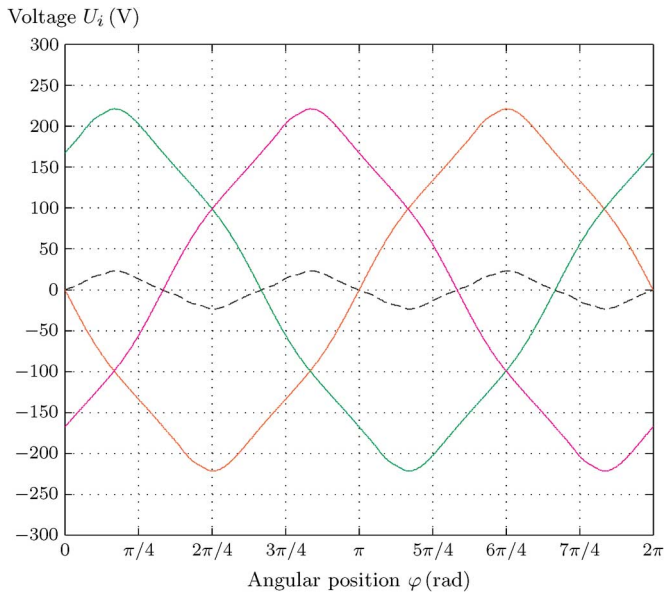


Fig. 7. No-load voltages of the three phases (solid lines) and zero sequence voltage (dashed line), rated speed of $n = 400$ rpm, coupled phases.

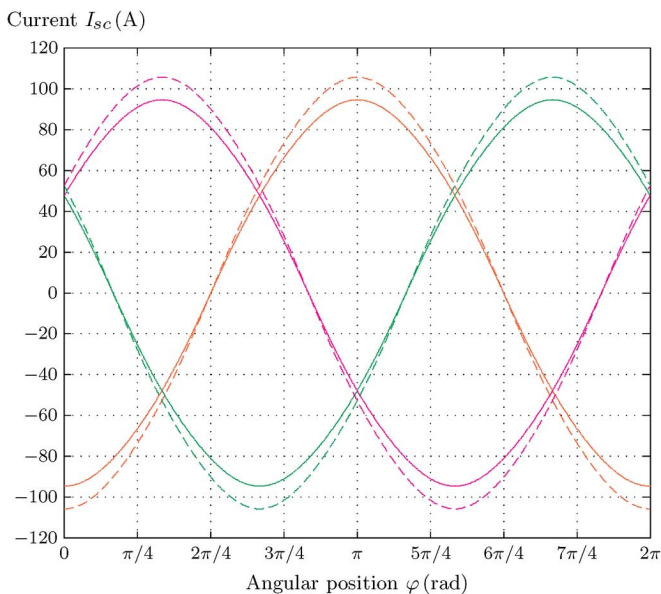


Fig. 8. Short-circuit currents of the three phases, rated speed of $n = 400$ rpm, decoupled phases (dashed lines) and coupled phases (solid lines).

of the rotor. The various angular rotor positions are analyzed without any remeshing of air-gap regions by utilizing domain decomposition and static condensation in the nonlinear calculations.

The presented results are focussed on the most important parameters such as electromagnetic torque, no-load voltage and short-circuit current of this novel prototype design. First measurement results obtained from an initial design show a good agreement with the numerical results discussed herein.

REFERENCES

- [1] A. Lange, W. R. Candors, F. Laube, and H. Mosebach, "Comparison of different drive systems for a 75 kW electrical vehicle drive," presented at the Int. Conf. Electrical Machines, ICEM, Espoo, Finland, 2000.
- [2] P. Anpalahan, "Design of Transverse flux machines using analytical calculations and finite element analysis," Licentiate of Technology thesis, Royal Inst. Technol., Stockholm, Sweden, 2001.
- [3] R. Blissenbach, "Entwicklung von permanentregerten transversalfussmaschinen hoher drehmomentdichte für traktionsantriebe," (in German) Doctoral thesis, RWTH, Aachen, Germany, 2002.
- [4] W. Hackmann, "Systemvergleich unterschiedlicher radnabenantriebe für den schienenverkehr: asynchronmaschine, permanenterrege synchronmaschine, transversalfussmaschine," (in German) Doctoral thesis, TU, Darmstadt, Germany, 2003.
- [5] A. Njeh, A. Masmoudi, and A. Elantably, "3D finite element analysis based investigation of the cogging torque of a claw pole transverse flux permanent magnet machine," presented at the IEEE Int. Conf. Electric Machines and Drives, IEMDC, Madison, WI, 2003.
- [6] E. Schmidt, "3D finite element analysis of the cogging torque of a transverse flux machine," *IEEE Trans. Magn.*, vol. 41, no. 5, May 2005.
- [7] O. Biro, K. Preis, and K. R. Richter, "On the use of the magnetic vector potential in the nodal and edge finite element analysis of 3D magneto-static problems," *IEEE Trans. Magn.*, vol. 32, no. 3, May 1996.
- [8] K. Hameyer and R. Belmans, *Numerical Modelling and Design of Electrical Machines and Devices*. Southampton, U.K.: WIT Press, 1999.
- [9] J. Jin, *The Finite Element Method in Electromagnetics*. New York: Wiley, 2002.
- [10] H. De Gersem, J. Gyselinck, P. Dular, K. Hameyer, and T. Weiland, "Comparison of sliding surface and moving band techniques in frequency-domain finite element models of rotating machines," presented at the 6th Int. Workshop Electric and Magnetic Fields, EMF, Aachen, Germany, 2003.
- [11] H. De Gersem and T. Weiland, "Harmonic weighting functions at the sliding surface interface of a finite element machine model incorporating angular displacement," *IEEE Trans. Magn.*, vol. 40, no. 2, Mar. 2004.